

RESEARCH ARTICLE | MARCH 20 2023

# A pre-time-zero spatiotemporal microscopy technique for the ultrasensitive determination of the thermal diffusivity of thin films <sup>EP</sup>

Sebin Varghese <sup>ID</sup> ; Jake Dudley Mehew <sup>ID</sup> ; Alexander Block <sup>ID</sup> ; David Saleta Reig <sup>ID</sup> ; Paweł Woźniak <sup>ID</sup> ; Roberta Farris <sup>ID</sup> ; Zeila Zanolli <sup>ID</sup> ; Pablo Ordejón <sup>ID</sup> ; Matthieu J. Verstraete <sup>ID</sup> ; Niek F. van Hulst <sup>ID</sup> ; Klaas-Jan Tielrooij <sup>ID</sup>

 Check for updates

Rev. Sci. Instrum. 94, 034903 (2023)  
<https://doi.org/10.1063/5.0102855>

  
View  
Online

  
Export  
Citation

CrossMark



[www.ssi-instrument.com](http://www.ssi-instrument.com)

- PXIe module Lock-in Amplifier
- Multi-channel Lock-in Amplifier
- Up to 8 demodulators
- Toolset: Scope, FFT, PID, Sweeper

## Customize your own Lock-in Amplifier

DC to 300MHz frequency



# A pre-time-zero spatiotemporal microscopy technique for the ultrasensitive determination of the thermal diffusivity of thin films

Cite as: Rev. Sci. Instrum. 94, 034903 (2023); doi: 10.1063/5.0102855

Submitted: 13 June 2022 • Accepted: 2 March 2023 •

Published Online: 20 March 2023











View Online



Export Citation



CrossMark

Sebin Varghese,<sup>1</sup>  Jake Dudley Mehew,<sup>1</sup>  Alexander Block,<sup>1</sup>  David Saleta Reig,<sup>1</sup>  Paweł Woźniak,<sup>2</sup>   
Roberta Farris,<sup>1</sup>  Zeila Zanolli,<sup>3</sup>  Pablo Ordejón,<sup>1</sup>  Matthieu J. Verstraete,<sup>4</sup>  Niek F. van Hulst<sup>2,5</sup>   
and Klaas-Jan Tielrooij<sup>1,a)</sup> 

## AFFILIATIONS

<sup>1</sup>Catalan Institute of Nanoscience and Nanotechnology (ICN2), BIST & CSIC, Campus UAB, Bellaterra (Barcelona) 08193, Spain

<sup>2</sup>ICFO-Institut de Ciències Fòniques, The Barcelona Institute of Science and Technology, 08860 Castelldefels, Barcelona, Spain

<sup>3</sup>Chemistry Department and ETSF, Debye Institute for Nanomaterials Science, Utrecht University, Utrecht, The Netherlands

<sup>4</sup>Nanommat, Q-Mat, CESAM, and European Theoretical Spectroscopy Facility, Université de Liège, B-4000 Liège, Belgium

<sup>5</sup>ICREA-Institució Catalana de Recerca i Estudis Avançats, 08010 Barcelona, Spain

<sup>a)</sup> Author to whom correspondence should be addressed: [klaas.tielrooij@icn2.cat](mailto:klaas.tielrooij@icn2.cat)

## ABSTRACT

Diffusion is one of the most ubiquitous transport phenomena in nature. Experimentally, it can be tracked by following point spreading in space and time. Here, we introduce a spatiotemporal pump–probe microscopy technique that exploits the residual spatial temperature profile obtained through the transient reflectivity when probe pulses arrive before pump pulses. This corresponds to an effective pump–probe time delay of 13 ns, determined by the repetition rate of our laser system (76 MHz). This pre-time-zero technique enables probing the diffusion of long-lived excitations created by previous pump pulses with nanometer accuracy and is particularly powerful for following in-plane heat diffusion in thin films. The particular advantage of this technique is that it enables quantifying thermal transport without requiring any material input parameters or strong heating. We demonstrate the direct determination of the thermal diffusivities of films with a thickness of around 15 nm, consisting of the layered materials MoSe<sub>2</sub> (0.18 cm<sup>2</sup>/s), WSe<sub>2</sub> (0.20 cm<sup>2</sup>/s), MoS<sub>2</sub> (0.35 cm<sup>2</sup>/s), and WS<sub>2</sub> (0.59 cm<sup>2</sup>/s). This technique paves the way for observing nanoscale thermal transport phenomena and tracking diffusion of a broad range of species.

© 2023 Author(s). All article content, except where otherwise noted, is licensed under a Creative Commons Attribution (CC BY) license (<http://creativecommons.org/licenses/by/4.0/>). <https://doi.org/10.1063/5.0102855>

## INTRODUCTION

Pump–probe measurements, where a probe pulse interrogates a system at a variable time delay after the system has been excited by a pump pulse, are powerful and versatile techniques to obtain information on dynamical processes with high temporal resolution and high sensitivity. In spatiotemporal pump–probe measurements,<sup>1–7</sup> pump and probe pulses have a variable relative offset in space, in addition to their variable time delay. Typically, one of the beams is scanned over the other, fixed beam, providing information on spatiotemporal transport phenomena, such as diffusion. Most commonly, one observes the broadening of an

initially pump-excited spot as a function of pump–probe time delay  $\Delta t$ , where the probe arrives later than the pump. The accuracy in resolving spatial broadening is determined by the signal-to-noise ratio and can therefore be significantly beyond the diffraction limit. Recently, this super-resolution technique has gained increasing attention as an important tool for studying diffusion in semiconductors,<sup>1,2</sup> organic compounds,<sup>4</sup> perovskites,<sup>6,7</sup> metals,<sup>5</sup> two-dimensional materials,<sup>3,8</sup> and more. However, with current spatiotemporal pump–probe techniques, it is challenging to resolve processes with low diffusivities.

One specific slow diffusion process, in comparison with electronic diffusion, is the phonon heat diffusion that governs the

lattice thermal conductivity.<sup>9</sup> Understanding thermal transport is extremely important, in particular, when materials are used in technological applications: avoiding (local) overheating is crucial for proper device operation and prolonged device lifetimes in electronic, optical, and optoelectronic devices and systems.<sup>10</sup> However, it is highly challenging for spatiotemporal techniques based on pump–probe measurements to resolve thermal diffusion because of the limited amount of spatial broadening. Silicon, for example, has a thermal diffusivity  $D$  of around  $1 \text{ cm}^2/\text{s}$ .<sup>11</sup> If heat is deposited by a pump pulse in a Gaussian spot with a width  $\sigma_{\Delta t=0}$ , the two-dimensional spatial broadening as a function of pump–probe delay time  $\Delta t$  is described by the diffusion equation:  $\sigma_{\Delta t>0}^2 = \sigma_{\Delta t=0}^2 + 2D\Delta t$ . This means that with an initial spot size of  $1 \text{ }\mu\text{m}$ , after 100 ps, the broadening due to thermal diffusion in silicon is just a few nanometers. Moreover, most materials have a lower diffusivity than silicon and, therefore, show even less spatial broadening. Alternative optical techniques to measure thermal transport typically obtain thermal conductivity rather than diffusivity, require accurate knowledge of several material and interface parameters, and/or need relatively strong heating of tens to hundreds of Kelvin. Moreover, the thermal diffusivities of even the most typical transition metal dichalcogenide (TMD) thin films— $\text{MoSe}_2$ ,  $\text{WSe}_2$ ,  $\text{MoS}_2$ , and  $\text{WS}_2$ —have not yet been obtained in a direct experimental way. Finally, there is no strong consensus on the values of the thermal conductivity of these systems, in particular, toward the monolayer limit, neither in experiments nor calculations. Novel experimental techniques could provide useful insights into solving this debate.

Here, we introduce pre-time-zero spatiotemporal microscopy as a technique that enables the direct determination of the diffusivity of long-lived excitations by examining the spatial profile at a small negative pump–probe delay time, where the probe arrives before the pump. In this configuration, the probe is sensitive to the residual signal generated by previous pump pulses from the incident pulse train. For example, with a repetition rate  $f_{\text{rep}}$  of 76 MHz, the pre-time-zero signal corresponds to an effective time delay of  $\Delta t \approx 13 \text{ ns}$ . We demonstrate the strengths of this technique by quantifying the in-plane thermal diffusivity  $D$  of free-standing thin films of the TMD material family. We use suspended films, such that phonon heat can accumulate due to the absence of a heat-sinking substrate. Furthermore, the temperature sensitivity reaches the sub-Kelvin level, when probing with a wavelength close to the exciton resonance, where the reflection is particularly sensitive to lattice temperature. We obtain thermal diffusivity directly by comparing the experimental spatial profile to a simple model based on Fourier's law of heat conduction, which does not require any material input parameters. The obtained experimental results are in agreement with our *ab initio* simulations based on density functional theory (DFT) and with experimental values in the literature. We will discuss the advantages of this technique and provide an outlook of the important studies this technique enables, in terms of (nanoscale) thermal transport, and beyond.

## RESULTS

### Concept and implementation of pre-time-zero spatiotemporal microscopy

We explain the fundamental idea behind our pre-time-zero spatiotemporal technique, and the experimental setup; see Fig. 1(a).

An optical pump pulse excites a small region of the sample. Initially, the spatial distribution of the excited species corresponds to the profile of the tightly focused pump beam. As the excited species diffuse, the profile broadens spatially. In the case that the diffusing excitation lives long enough for a new pump pulse to arrive before the system has returned to equilibrium, we can monitor the spatially broadened profile using a probe pulse at a small negative pump–probe time delay. This delay time thus corresponds to a delay that is roughly equal to the temporal spacing between subsequent pump pulses. This enables the study of spatial broadening occurring over a longer timescale than the conventional pump–probe delay time.

Whereas the concept is generally applicable to any long-lived excitations, we now focus on the specific case of quantifying thermal transport in thin films, in order to demonstrate the strengths of pre-time-zero spatiotemporal pump–probe microscopy. We exploit the notion that a pump-induced electronic excitation relaxes over time, typically transferring energy to the lattice subsystem, where phonons carry the energy as heat. Furthermore, we use the idea that heat changes the optical properties of a material, which we detect with our probe pulses. Since the pump–probe measurements enable the observation of very small pump-induced changes in transmission or reflection, this technique can detect small amounts of heat, which we will quantify below. We fix the position of the pump beam and scan the probe beam in the sample plane, resolving the spatial profile of the transient reflectivity signal  $\frac{\Delta R}{R}$  (detected using a silicon photodiode) as a function of spatial pump–probe offset  $\Delta x$  and/or  $\Delta y$ . Here, transient reflectivity is  $\frac{\Delta R}{R} = \frac{R_{\text{exc}} - R}{R}$ , where  $R_{\text{exc}}$  and  $R$  are the reflections of the probe with and without the pump pulse, respectively. By scanning the position of the probe beam with respect to the pump beam with nanometer precision, we acquire accurate spatial transient reflectivity maps  $\frac{\Delta R}{R}(\Delta x, \Delta y)$ . We will show that the transient reflectivity profile represents the temperature profile  $\Delta T(\Delta x, \Delta y)$ , which enables us to extract the thermal diffusivity.

In our specific experimental setup (see the [supplementary material](#), Fig. S1), a mode-locked laser ( $f_{\text{rep}} = 76 \text{ MHz}$ ) generates pulses centered at 1030 nm. Most of the laser output power is used to pump an optical parametric oscillator (OPO) that has a tunable signal output between 1320 and 2000 nm. The probe beam is either the second or the third harmonic of the signal output, depending on the sample under investigation. We direct the probe via a scanning mirror system (Optics in Motion OIM101) while the pump beam (515 nm, second harmonic of the fundamental laser source) goes onto a variable delay line (Newport DL225) and an optical chopper that regulates the pump modulation frequency  $f_{\text{mod}}$ . Both beams combine via a dichroic mirror and focus on sub-micrometer spot sizes via a microscope objective lens (numerical aperture: 0.67).

Figures 1(b) and 1(c) show exemplary transient reflectivity maps recorded at two pump–probe time delays  $\Delta t$ . At time-zero ( $\Delta t = 0$ ), we observe a narrow profile centered at the pump spot  $\Delta x = \Delta y = 0$ , which is due to the electronic excitation induced by absorption of the pump pulse [see Fig. 1(b)]. The spatial profile looks very different when tuning to a small negative time delay  $\Delta t < 0$ , i.e., pre-time-zero, typically a few picoseconds before time-zero. Here, we observe a broader profile with a smaller amplitude [see Fig. 1(c)]. We attribute this signal to diffused phonon heat in the sample. The broader the pre-time-zero profile, the larger we expect the diffusivity

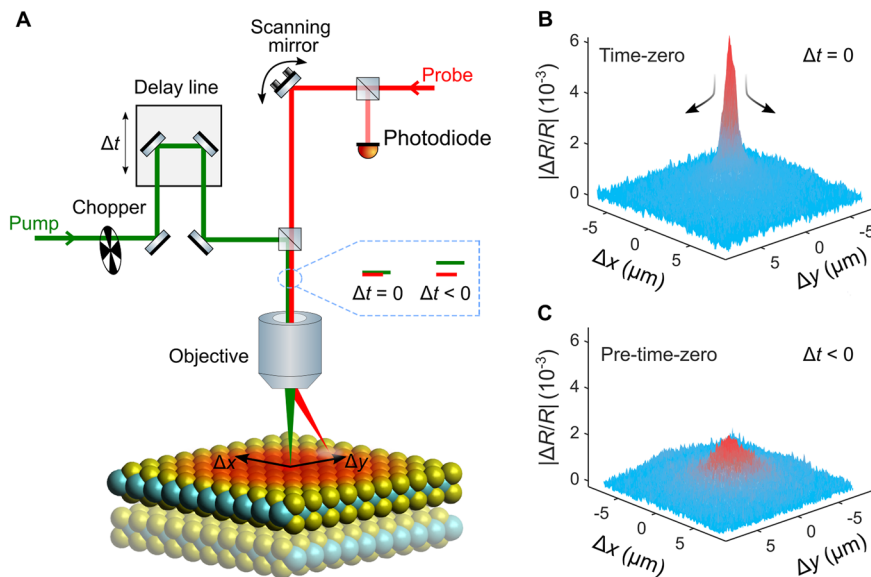


**FIG. 1.** Schematic representation of the spatiotemporal pump-probe microscopy setup. (a) An optical pump pulse is focused onto the sample, creating a local excitation. To monitor the diffusion of this excitation, a probe beam scans spatially over the sample around the pump spot. The modulated pump beam passes over a delay line that controls the time delay  $\Delta t$  between the pulses. The probe beam position at the sample plane is controlled by a scanning mirror. Both beams are combined with a dichroic mirror and focused onto the sample through an objective. The reflected probe beam is detected using a silicon photodiode and demodulated at the modulation frequency, typically in the kHz range. A detailed schematic is shown in the [supplementary material](#), Fig. S1. (b) The transient reflectivity profile  $\frac{\Delta R}{R}(\Delta x, \Delta y)$  at a time delay  $\Delta t = 0$  (time-zero) shows a narrow profile that corresponds to the purely electronic response created by photoexcitation from the pump pulse. (c) The profile measured at a small negative time delay  $\Delta t < 0$  (pre-time-zero) shows a broadened response due to the diffusion of excitation created by previous pump pulses. Effectively, this corresponds to a pump-probe delay that is equal to the inverse of the laser repetition rate, typically in the nanosecond regime. As explained in detail in the text, the pre-time-zero signal reflects a temperature-dependent electronic response, which allows us to observe heat spreading.

of the phonon heat to be, and this eventually allows us to obtain the diffusivity quantitatively.

### Spatiotemporal pump-probe measurements on TMDs

We apply our spatiotemporal technique to a prototypical thin-film system: transition metal dichalcogenide crystals. Like graphite, TMDs are layered crystals with strong in-plane bonds between atoms, while adjacent layers are weakly bound by van der Waals forces. They have attracted significant interest in recent years due to their many intriguing optical,<sup>12</sup> electrical,<sup>13</sup> mechanical,<sup>14</sup> and thermal properties.<sup>15</sup> A thorough understanding of their thermal properties is crucial to enable technologies, including (opto)electronic, thermoelectric, medical, and thermal management applications. Whereas their thermal conductivities  $\kappa$  have been obtained experimentally, their thermal diffusivities  $D$  have not been determined directly, even though the diffusivity arguably describes thermal transport more directly. We study free-standing films of MoSe<sub>2</sub>, WSe<sub>2</sub>, MoS<sub>2</sub>, and WS<sub>2</sub>, of thickness around 15 nm, corresponding to  $\sim 20$  layers, suspended over gold-coated substrates with circular holes with a diameter of 15  $\mu\text{m}$  (Norcada, NTPR005D-C15). The sample fabrication, based on polydimethylsiloxane (PDMS)-assisted dry transfer of mechanically exfoliated TMDs (purchased from HQ graphene), is described in detail elsewhere.<sup>16</sup> To facilitate efficient heat sinking outside the suspended area, we coated

the substrate with 5/50 nm of Ti/Au. The measurements are performed in air (and at room temperature), as going to vacuum led to negligibly small differences (see the [supplementary material](#), Fig. S2).

Figures 2(a) and 2(b) show the transient reflectivity signal on suspended and supported regions of the flakes, as a function of pump-probe delay time. In both regions, the signal peaks at  $\Delta t = 0$  ps. This is associated with the photoexcitation of charge carriers and sub-picosecond exciton formation.<sup>3</sup> We first examine the substrate-supported region, where the signal decays over picosecond timescales and can be understood as a decrease in exciton population.<sup>17</sup> The pump-probe signal decays to a value very close to zero during the time window provided by our delay line (150 ps) and is zero after  $\sim 13$  ns, as observed in the pre-time-zero signal. This means that the system is in equilibrium before the next pump pulse arrives. In the suspended region, in contrast, there is a clear remnant signal before time zero [see Figs. 2(a) and 2(b)]. We ascribe this signal to phonon heat that has accumulated in the sample. This does not occur in the supported regions due to efficient out-of-plane heat sinking to the gold-coated substrate.

In order to confirm that the pre-time-zero signal corresponds to a phonon-heat induced change in the reflection of our probe, we measure the signal as a function of probe wavelength [see Fig. 2(c)]. We observe a clear peak at a wavelength of 635, 675, 770, and 805 nm that corresponds to the A-exciton resonance of WS<sub>2</sub>, MoS<sub>2</sub>, WSe<sub>2</sub>, and MoSe<sub>2</sub>, respectively.<sup>18–20</sup> We describe the experimental

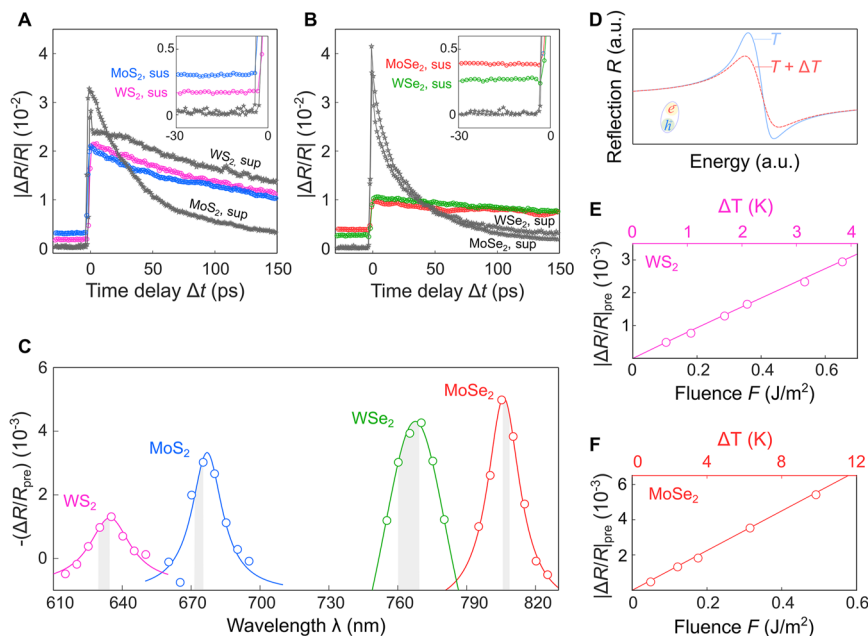


**FIG. 2.** Pre-time-zero spatiotemporal experiment. Comparison of absolute transient reflectivity  $|\frac{\Delta R}{R}|$  dynamics in suspended (sus) and supported (sup) regions of WS<sub>2</sub> and MoS<sub>2</sub> (a), WSe<sub>2</sub> and MoSe<sub>2</sub> (b). Insets show a zoomed-in view of the signal before time zero. (c) Pre-time-zero reflectivity signal  $-(\frac{\Delta R}{R})_{\text{pre}}$  measured at different probe wavelengths with a constant incident pump fluence of  $\sim 0.3 \text{ J/m}^2$ . The largest response corresponds to the A exciton resonance of the materials. The solid line is a Lorentzian fit to the data. The shaded area represents typical A exciton peaks found in the literature. (d) Simulated reflection spectrum around an exciton resonance at two different temperatures. (e) and (f) Magnitude of the pre-time-zero signal as a function of pump fluence (circles, bottom axis) and temperature rise (solid line, top axis) for WS<sub>2</sub> (e) and MoSe<sub>2</sub> (f) extracted from the Lorentz oscillator model. For (c), (e), and (f), we average  $\sim 50$  data points at different negative time delays from an interval of a few picoseconds. The error bars are smaller than the marker size (68% confidence interval), and the exponent of a power law fit these data is 0.98 (e) and 0.99 (f), indicating that the relationship is very close to linear.

data with a Lorentzian function and extract linewidths of 21 nm (WS<sub>2</sub>), 16 nm (MoS<sub>2</sub>), 44 nm (WSe<sub>2</sub>), and 17 nm (MoSe<sub>2</sub>), similar to the literature reports of exciton linewidths.<sup>21</sup> It is known that these linewidths are temperature dependent,<sup>22</sup> which provides the physical connection between the measured optical response and phonon heat in the sample: Figure 2(d) shows a representative reflection profile obtained from the Lorentz oscillator model (see the supplementary material, Note 1) at two different phonon temperatures. With an increased lattice temperature, the exciton linewidth increases, and this leads to a decrease in reflection, which is what we observe.

We examine this in more detail by measuring the transient reflectivity signal as a function of pump fluence  $F$  [see Figs. 2(e) and 2(f)] in WS<sub>2</sub> and MoSe<sub>2</sub>. The first thing we notice is the linear dependence of the transient reflectivity  $\frac{\Delta R}{R}$  on fluence (also see the supplementary material, Fig. S3). Importantly, this justifies the use of the transient reflectivity profile  $\frac{\Delta R}{R}(\Delta x, \Delta y)$  as a representative of the temperature profile  $\Delta T(\Delta x, \Delta y)$ , from which we will extract the diffusivity. Second, we extract the temperature increase  $\Delta T$  from the observed transient reflectivity and compare this to the expected  $\Delta T$  based on pulse energy and heat capacity. For this, we use the complex dielectric function of WS<sub>2</sub> and MoSe<sub>2</sub> according to a Lorentz oscillator model of the exciton resonance (see the supplementary material, Note 1), and the temperature-dependent exciton linewidth from Ref. 22, finding values below 10 K up to the largest applied fluence

[see Figs. 2(e) and 2(f)]. We compare this extracted  $\Delta T$  to the peak temperature increase using the relation  $\Delta T_{\text{peak}} = (A \cdot F)/(h \cdot C_v)$ , where  $A$  is the absorption (see the supplementary material, Fig. S4),  $h$  is the thickness, and  $C_v$  is the heat capacity, finding good agreement. A fluence of  $0.4 \text{ J/m}^2$ , for example, in WS<sub>2</sub> (MoSe<sub>2</sub>) corresponds to a  $\Delta T \sim 2 \text{ K}$  ( $\sim 8 \text{ K}$ ) from the Lorentz model [see Figs. 2(e) and 2(f)] and a peak temperature rise of  $\Delta T_{\text{peak}} \sim 3 \text{ K}$  ( $\sim 5 \text{ K}$ ), using  $h = 17.2 \text{ nm}$  (13.8 nm), and  $C_v$  from literature (WS<sub>2</sub> from Ref. 23 and MoSe<sub>2</sub> from Ref. 24). Importantly, these results show that the technique is sensitive to reflection changes caused by heating by less than a Kelvin.

Having established that our probe is highly sensitive to phonon heat via the exciton linewidth, we now examine the  $\Delta t < 0$  spatial profiles at different pump modulation frequencies ( $f_{\text{mod}}$ ) between 4 and 240 kHz, as controlled by an optical chopper or an electro-optic modulator. We position the pump beam in the center of the suspended region of the sample and scan the probe beam with respect to the pump spot at  $\Delta t = 0$  and at a small negative time delay ( $\Delta t < 0$ ), with a pump fluence of  $\sim 0.3 \text{ J/m}^2$ . Figure 3(a) shows the normalized  $\frac{\Delta R}{R}$  spatial profiles acquired at  $\Delta t = 0$  and  $\Delta t < 0$  for MoSe<sub>2</sub>. For the  $\Delta t = 0$  profile, we subtracted the  $\Delta t < 0$  background signal (see the supplementary material, Fig. S5), and find that it is accurately described using a Gaussian function [Fig. 3(a)], which corresponds to a convolution of our pump and probe spot sizes (see the supplementary material, Fig. S6 and Note 2). We



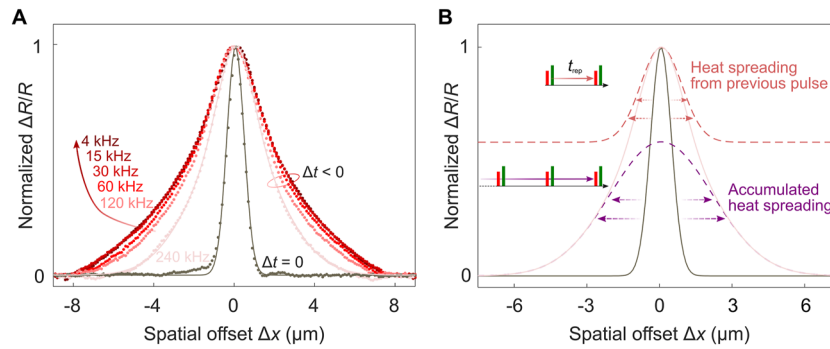


**FIG. 3.** Spatial profiles at varying modulation frequencies for MoSe<sub>2</sub>. (a) Spatial profiles  $\Delta t < 0$  for different modulation frequencies. For low modulation frequencies (4–30 kHz), the spatial profiles are similar, indicating temperature saturation due to steady state formation. The solid line for  $\Delta t < 0$  profile (240 kHz) is the description of the data by the sum of two Gaussians. The narrow profile represents the corresponding  $\Delta t = 0$  profile (gray data points) and is described by a single Gaussian function. (b) Description of the spatial profile with 240 kHz modulation at  $\Delta t = 0$  (gray line, single Gaussian) and  $\Delta t < 0$  (light red line, sum of two Gaussians). The narrow dashed Gaussian (offset vertically) represents the resulting profile due to heat spreading from the previous pump pulse. The broad Gaussian is the resulting profile due to accumulative heat spreading from all the previous pump pulses. By analyzing the width of the  $\Delta t = 0$  profile and the width of the narrow Gaussian, we obtain a  $D$  of 0.21 cm<sup>2</sup>/s. All profiles are normalized to the peak of the fit.

observe that the  $\Delta t < 0$  spatial profiles broaden with decreasing  $f_{\text{mod}}$  and tend to saturate for the lowest modulation frequencies [see Fig. 3(a)]. This saturation is due to the formation of a steady-state profile and is understood as follows: The rate with which heat that is added to the material by absorbed light from the pump pulses is equal to the rate with which heat diffuses to the edge of the suspended material and heat-sinks into the gold-coated substrate. These spatial profiles can be described by two Gaussians: The narrow component corresponds to the diffused heat from the previous pump pulse and is, therefore, associated with a timescale of  $1/f_{\text{rep}} = 13$  ns. The broader component corresponds to accumulated heat spreading from all the previous pump pulses and is therefore associated with a timescale of  $1/f_{\text{mod}} = 4\text{--}250$   $\mu\text{s}$ . For lower modulation frequencies, corresponding to longer excitation with pump pulses, there is more accumulated heat, making the profile broader. We analyze the spatial profile taken at 240 kHz and use its narrow component to estimate the thermal diffusivity  $D$  of the sample. This is done by comparing the Gaussian width ( $\sigma_{\Delta t=0}$ ) of the spatial profile at  $\Delta t = 0$  and the Gaussian width ( $\sigma_{\Delta t<0,\text{narrow}}$ ) of the narrow part of the  $\Delta t < 0$  profile. The diffusivity is then given by  $D = [\sigma_{\Delta t<0,\text{narrow}}^2 - \sigma_{\Delta t=0}^2]/2\Delta t$ . Using  $\Delta t = 13$  ns, we obtain a  $D$  of 0.21 cm<sup>2</sup>/s [see Fig. 3(b)]. We will show below that this is a very reasonable estimate.

### Simulations of the pre-time-zero spatiotemporal technique

In order to more accurately quantify the diffusivity and understand the spatial profiles, we schematically show the evolution of the temperature rise in the suspended region of the sample during one pump modulation period [Fig. 4(a)]. When the pump beam is not blocked, a pulse train photoexcites and locally heats the sample. Since the system does not return to equilibrium before the next pump pulse arrives, heat continuously accumulates in the system, which is excited by  $N = f_{\text{rep}}/2f_{\text{mod}}$  pump pulses (50% duty cycle modulation). Consequently, the system temperature increases,

reaching a maximum at the end of these  $N$  pump pulses. The accumulated heat then decays when the pump pulses are blocked, and the system reaches thermal equilibrium before the next period with  $N$  pump pulses.

The evolution of the spatial reflectivity profiles, which correspond to temperature profiles, is shown in Fig. 4(b). After the first pump pulse, the initial photoexcitation at pump-probe delay time  $\Delta t = 0$  has a narrow Gaussian profile [see profile (i)]. After pump excitation and electron-phonon coupling, the heat in the phonon system starts diffusing. Therefore, at a small negative  $\Delta t$ , just before the next pump pulse arrives, the Gaussian profile broadens [see profile (ii)]. The second pump pulse then adds a narrow Gaussian profile on top of the broadened Gaussian profile [see profile (iii)]. This profile then diffuses, leading to a sum of two broadened Gaussians [see profile (iv)]. This process continues for  $N$  pump pulses, leading to profile (v), just after the last pump pulse. The cumulative photoexcitation after  $N$  pulses finally results in a spatial profile as in (vi). This profile contains a narrow component that corresponds to the diffused heat from the previous pump pulse and a broader component that corresponds to the accumulated heat from all previous pump pulses. The latter tends to the triangular steady-state solution for continuous heating and cooling through diffusion to a perfect heat sink, which is the gold-coated substrate located at 7.5  $\mu\text{m}$  from the center of the suspended region.

To understand the shape of the spatial profile quantitatively and to obtain an accurate thermal diffusivity, we perform a simple simulation based on Fourier's law of heat conduction,

$$\frac{\partial T}{\partial t} = D \left( \frac{\partial^2 T}{\partial x^2} + \frac{\partial^2 T}{\partial y^2} \right),$$

where  $T$  is temperature,  $t$  is time,  $x$  and  $y$  are the spatial coordinates, and  $D$  is the thermal diffusivity of the material. We calculate the two-dimensional diffusion with radial symmetry and obtain the temperature increase  $\Delta T(x, y)$ . As the boundary condition, we use a perfect heat sink at the edge of the circular sample with radius  $r_0$ .

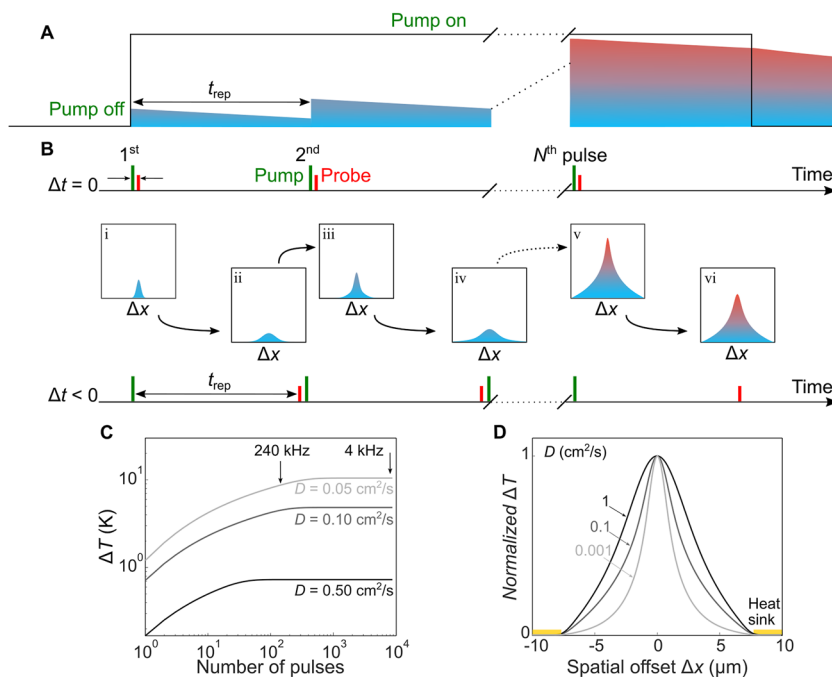


**FIG. 4.** Simulations of pre-time-zero profiles. (a) Heat accumulation in the free-standing region of the sample as a function of time, during one pump modulation period. (b) Spatial heat profiles directly after the first pump pulse (i), after the heat of the first pump pulse has diffused (ii), directly after the second pump pulse (iii), after the combined heat of the first two pulses has diffused (iv), directly after the  $N$ th pump pulse (v), and after the combined heat of  $N$  pulses has diffused (vi). By using a negative pump–probe delay time, the  $N$ th probe pulse senses the effect of the  $(N - 1)$ th pump pulse. [(c) and (d)] Simulation results obtained from a straightforward Fourier heat diffusion model, as explained in the main text. (c) Temperature increase  $\Delta T$  as a function of the number of pulses  $N$  for different input diffusivities  $D$ . (d) Normalized average spatial heat profiles after  $N$  pulses for a range of  $D$ . Broader average profiles correspond to higher diffusivities.

Thus, at position  $r = \sqrt{x^2 + y^2}$ , we have  $\Delta T|_{r=r_0} = 0$  K. In the simulation, we let an initial Gaussian temperature increase evolve in space and time with a fixed diffusion coefficient. At  $t = 1/f_{\text{rep}}$ , we add another pump pulse to the remnant heat profile. We repeat this for all  $N$  pulses and obtain the final spatial temperature profile. For increasing  $N$ , we find the occurrence of saturation of the peak temperature at  $\Delta x = 0$ , related to the formation of a steady-state profile, see Fig. 4(c). This is in agreement with our experimental observation [Fig. 3(a)] that the spatial profile does not change for the lowest modulation frequencies (larger number of pulses). The simulations indicate that with a higher diffusivity fewer pulses are needed to reach a steady-state situation, and the resulting peak temperature is lower. This is because in this case heat diffuses more quickly to the heat sink.

As a final simulation result, we show how the spatial profile changes for different diffusivities. This is important, as it indicates how sensitive our technique is toward obtaining the diffusivity of a sample, and how large a range of diffusivities can be obtained. For this, we performed simulations with different diffusion coefficients and plot the resulting average spatial profile after  $N$  pulses [see Fig. 4(d)]. Our simulations show that the average spatial profiles get broader for larger  $D$ , verifying our earlier intuitive explanation. Furthermore, we see that this technique is capable of obtaining diffusivities varying over several orders of magnitude.

### Obtaining and evaluating the thermal diffusivities of TMDs

We quantify the thermal diffusivity  $D$  of four different TMD samples. We use a modulation frequency of 4.37 kHz, in order to be in the saturation regime, where the spatial profile does not depend

on modulation frequency. Figures 5(a)–5(d) show the normalized  $\Delta t = 0$  and  $\Delta t < 0$  spatial profiles for  $\text{MoSe}_2$  (a),  $\text{WSe}_2$  (b),  $\text{MoS}_2$  (c), and  $\text{WS}_2$  (d), measured at a pump fluence of  $\sim 0.3$   $\text{J}/\text{m}^2$ . The extracted diffusivity is the one that minimizes the squared residuals between the experimental pre-time-zero profile and the simulated profile. The only parameters we need for this are the diameter of the suspended flake ( $15$   $\mu\text{m}$  by design) and the experimental beam width of the pump and the probe (see the supplementary material, Note 2). In order to match the experimental conditions, we convolute the obtained profiles with the probe beam spatial profile. Using this procedure, we obtain thermal diffusivities  $D$  of  $0.18 \pm 0.02$   $\text{cm}^2/\text{s}$  for  $\text{MoSe}_2$ ,  $0.20 \pm 0.03$   $\text{cm}^2/\text{s}$  for  $\text{WSe}_2$ ,  $0.35 \pm 0.04$   $\text{cm}^2/\text{s}$  for  $\text{MoS}_2$ , and  $0.59 \pm 0.07$   $\text{cm}^2/\text{s}$  for  $\text{WS}_2$ . The uncertainty in  $D$  comes from two contributions: a statistical error from the least-square fit of the data to the model (5%–10%) and a structural error mostly from the uncertainty of the spot sizes ( $\sim 5\%$ ) (see the supplementary material, Figs. S7 and S8).

In order to assess the validity of the obtained diffusivities for these TMD films, we first compare them to experimental values in the literature. Most studies report thermal conductivity ( $\kappa$ ), which relates to diffusivity ( $D$ ) via the heat capacity ( $C_V$ ):  $\kappa = D \cdot C_V$ . Therefore, we convert our diffusivity values using the bulk heat capacities of  $\text{MoSe}_2$  from Ref. 24,  $\text{WSe}_2$  from Ref. 31,  $\text{MoS}_2$  from Ref. 32, and  $\text{WS}_2$  from Ref. 23. Figure 5(e) shows the comparison of our experimental values (solid lines) to other experimental reports (symbols). We limit our comparison to literature values for relatively thick crystals of at least ten nanometers. We find good agreement between our results and those from literature, confirming the general trend that the selenides ( $\text{MoSe}_2$ ,  $\text{WSe}_2$ ) have a lower thermal conductivity than the sulfides ( $\text{MoS}_2$ ,  $\text{WS}_2$ ).<sup>15,33</sup> For bulk  $\text{MoSe}_2$  and  $\text{WSe}_2$ , other experimental studies show thermal

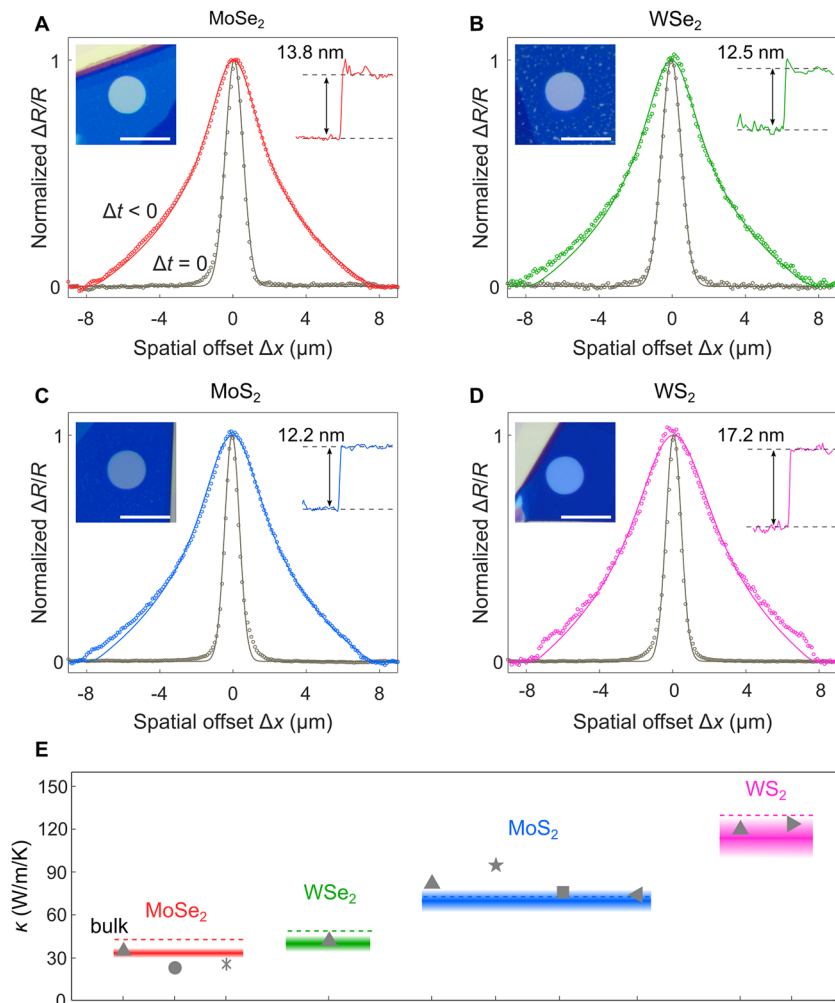


**FIG. 5.** Obtained thermal diffusivities and benchmarking. [(a)–(d)] Transient reflectivity  $\frac{\Delta R}{R}$  profiles for suspended MoSe<sub>2</sub> (a), WSe<sub>2</sub> (b), MoS<sub>2</sub> (c), and WS<sub>2</sub> (d), all normalized to the peak of the fit. The narrow profiles represent the time-zero profiles ( $\Delta t = 0$ ) and are described by Gaussian functions (solid gray lines) to extract their width. We obtain the thermal diffusivity ( $0.18 \pm 0.02 \text{ cm}^2/\text{s}$  for MoSe<sub>2</sub>,  $0.20 \pm 0.03 \text{ cm}^2/\text{s}$  for WSe<sub>2</sub>,  $0.35 \pm 0.04 \text{ cm}^2/\text{s}$  for MoS<sub>2</sub>, and  $0.59 \pm 0.07 \text{ cm}^2/\text{s}$  for WS<sub>2</sub>) by describing the pre-time-zero ( $\Delta t < 0$ ) profiles with our model based on heat diffusion (solid lines). The insets show the optical microscope image (left side, scale bar  $20 \mu\text{m}$ ) of the flakes, and atomic force microscopy profiles, from which we obtain the thickness (right side). (e) Obtained thermal conductivity ( $\kappa$ ) from the measured diffusivities compared with bulk experimental literature values:  $\triangle$  (Ref. 15),  $\circ$  (Ref. 25),  $*$  (Ref. 26),  $\star$  (Ref. 27),  $\square$  (Ref. 28),  $\triangleleft$  (Ref. 29), and  $\triangleright$  (Ref. 30). The thick line shows the obtained  $\kappa$  for our samples with a thickness of  $\sim 20$  layers, where the gradient limit represents the error bound with 95% confidence interval. The dashed lines represent our calculated  $\kappa$  for bulk.

conductivities ranging from  $22$  to  $42 \text{ W m}^{-1} \text{ K}^{-1}$ ,<sup>15,25,26</sup> which is in excellent agreement with our obtained  $\kappa$  of  $33.5 \text{ W m}^{-1} \text{ K}^{-1}$  for MoSe<sub>2</sub> and  $39.6 \text{ W m}^{-1} \text{ K}^{-1}$  for WSe<sub>2</sub> [Fig. 5(e)]. For WS<sub>2</sub>, we find a relatively large  $\kappa$  of  $113.9 \text{ W m}^{-1} \text{ K}^{-1}$ , which is in good agreement with experimental results.<sup>15,30</sup> Our value for MoS<sub>2</sub> of  $70 \text{ W m}^{-1} \text{ K}^{-1}$  is in good agreement with those reported in Refs. 15, 28, and 29. We do find a significantly lower thermal conductivity compared to the measured value in Ref. 27. This discrepancy is likely the result of the smaller thickness of our sample compared to the one in Ref. 27. Overall, we find good agreement between our experimentally obtained conductivities and the literature values.

We proceed with comparing our obtained values with calculated diffusivities using density functional theory at 300 K for bulk crystals, by using the SIESTA program and the temperature dependent effective potential (TDEP) method (see the supplementary material, Note 3 and Fig. S9 for details). We find that for all four TMDs the experimentally obtained conductivities follow the same qualitative trend as the calculations with  $\kappa_{\text{MoSe}_2} < \kappa_{\text{WSe}_2} < \kappa_{\text{MoS}_2} < \kappa_{\text{WS}_2}$ . Quantitatively, we find that our  $\sim 15 \text{ nm}$  thick films give slightly lower values than those calculated for bulk films. We

attribute this to the effect of the thickness, where thinner films typically have smaller thermal conductivities, cf. the recent combined experimental–theoretical work of Ref. 25. This suggests that  $15 \text{ nm}$  is a thickness where these layered materials do not yet behave completely bulk-like in terms of their thermal transport properties. Overall, we find good agreement between our measured results and those obtained through our calculations.

### Evaluation of the pre-time-zero spatiotemporal technique

We have seen that our pre-time-zero spatiotemporal technique allows for the accurate determination of the thermal diffusivities of thin films, and now discuss the main benefits of this technique. First of all, it offers the advantage of being a non-invasive, contact-free approach. Another main strength of the technique is that it enables the determination of the in-plane thermal diffusivity of a thin film by comparing the data to a simple description based on Fourier's heat law, where it does not require knowledge of any material parameters,



such as the temperature coefficient, optical absorption, thickness, interfacial thermal conductance, heat capacity, and/or properties related to transducer layers. The only input parameters we require for the simulations are very well-known experimental conditions: the diameter of the suspended region of the material, the repetition rate of the laser, and the spot sizes of the pump and probe beams. Since all these values are known within an error of a few percent or less, we obtain accurate diffusivities (see the [supplementary material](#), Fig. S7). Thus, the proposed method eliminates sources of error arising from necessary measurements of intermediate parameters that enter the model used for the extraction of unknown thermal properties.

Another important advantage is the sensitivity of the technique. The ability to observe changes in a spatial profile is limited only by the signal-to-noise ratio, which ultimately determines the accuracy of determining the diffusivity. Being a pump-probe technique, where the pump-induced changes are detected differentially using the combination of an optical chopper and a synchronized lock-in amplifier (Zurich Instruments MFLI), means that we can resolve very subtle heat-induced changes in permittivity (refractive index) of materials. As a result, it is possible to determine thermal transport properties even if the change in temperature due to heating is very small, on the single Kelvin level [see [Figs. 2\(e\)](#) and [2\(f\)](#)]. This is an important advantage over alternative techniques that require stronger heating.

Beyond offering these advantages, pre-time-zero spatiotemporal pump-probe microscopy will make it possible to explore previously inaccessible physical phenomena and properties. Continuing with thermal transport as the main example, we suggest combining our technique that provides the diffusivity with a complementary study that provides the thermal conductivity in order to obtain the heat capacity in an all-optical fashion. Our technique will also likely make it possible to access transport regimes where diffusive transport breaks down, and ballistic or hydrodynamic phonon transport occurs. These phenomena have been studied theoretically for two-dimensional materials;<sup>34,35</sup> however, there is minimal experimental evidence to support these reports.<sup>8,36</sup> As our technique is highly sensitive to diffusive processes that occur over nanometer length scales, we predict that it will facilitate an advance in the understanding of non-diffusive transport in low-dimensional materials. Furthermore, we point out that our technique enables the study of more complex structures, such as van der Waals heterostructures, consisting of combinations of different layered materials, with material specificity through the material-specific exciton resonances.

Finally, we discuss the limitations of pre-time-zero spatiotemporal microscopy. In our example of thermal diffusion in thin layered films, we benefit from an increased sensitivity due to the temperature-dependent exciton response. Not all materials exhibit exciton resonances and will therefore exhibit the same increased sensitivity. However, the technique will likely work for any diffusing species that has an optical response associated with it and that has a long enough lifetime to be detectable at a negative time delay. Since temperature-dependent refractive indices are very common, we expect that the thermal diffusivity of materials without an exciton response should also be attainable. Furthermore, we note that the thermal diffusivity might not be directly obtainable in all materials, such as materials with very long-lived photoexcited charges, because the pre-time zero signal will contain a significant

contribution that corresponds to electronic diffusion, rather than thermal diffusion. This, however, means that this technique makes it possible to observe charge diffusion in semiconducting thin films with nanosecond or microsecond carrier lifetimes, which is particularly interesting for such materials with low electronic diffusivities. Finally, we point out that our 2D diffusion model assumes uniform heating along the *c*-axis (out-of-plane), which is justified given the thicknesses of our flakes, which are smaller than the optical penetration depth. In the case of thicknesses larger than the optical penetration depth, combined with very low out-of-plane thermal conductivities (high thermal anisotropy), the 2D model will have to be modified into a 3D diffusion model.

## CONCLUSIONS

In this work, we have introduced a technique for measuring diffusion processes of long-lived excitations by exploiting the pre-time-zero spatial profile. In particular, we have shown that this technique can be used to obtain the in-plane thermal diffusivity of thin films. We have determined the thermal diffusivities of suspended MoSe<sub>2</sub>, WSe<sub>2</sub>, MoS<sub>2</sub>, and WS<sub>2</sub> thin films. Our technique provides a simple, sensitive, and accurate way of determining the thermal diffusivity, and will enable a deeper understanding of the thermal properties of nanoscale materials. Furthermore, the technique of pre-time-zero spatiotemporal scanning constitutes a powerful tool for studying a multitude of diffusion processes in a large variety of systems.

## SUPPLEMENTARY MATERIAL

See the [supplementary material](#) for the detailed schematic of pre-time-zero spatiotemporal setup (Fig. S1), comparison between measurements performed in ambient and vacuum environment (Fig. S2), the linear dependence of pre-time-zero signal with pump fluence (Fig. S3), absorption measurements on MoSe<sub>2</sub> and WS<sub>2</sub> at 515 nm pump wavelength (Fig. S4), background removal to obtain time-zero spatial profiles (Fig. S5), knife edge measurements of pump and probe beam to obtain spot sizes (Fig. S6), simulation to understand the effect of spot size in quantifying thermal diffusivity (Fig. S7), fitted pre-time-zero spatial profiles at different modulation frequencies (Fig. S8), convergence tests for density functional theory simulations on bulk MoSe<sub>2</sub> (Fig. S9), and the measurements performed on a 10  $\mu\text{m}$  suspended MoSe<sub>2</sub> sample (Fig. S10). Details of the Lorentz oscillator model, experimental beam width calculation, and density functional theory simulations are described in Note 1, Note 2, and Note 3, respectively.

## ACKNOWLEDGMENTS

ICN2 was supported by the Severo Ochoa program from Spanish MINECO Grant No. SEV-2017-0706. S.V. and D.S.R. acknowledge the support of the Spanish Ministry of Economy through FPI-SO2018 and FPI-SO2019, respectively. K.-J.T. acknowledges funding from the European Union's Horizon 2020 Research and Innovation program under Grant Agreement No. 804349 (ERC StG CUHL), RYC fellowship No. RYC-2017-22330 and IAE Project No. PID2019-111673GB-I00. ICFO was supported by the Severo Ochoa

program for Centers of Excellence in R&D (CEX2019-000910-S), Fundació Privada Cellex, Fundació Privada Mir-Puig, and the Generalitat de Catalunya through the CERCA program. P.W. acknowledges funding from the European Union's Horizon 2020 Research and Innovation program under the Marie Skłodowska-Curie Grant Agreement No. 754510 (PROBIST). N.F.v.H. acknowledges funding by the European Commission (ERC AdG 670949-LightNet), the Spanish Plan Nacional (PGC2018-096875-BI00), and the Catalan AGAUR (2017SGR1369). M.J.V. acknowledges support from Fédération Wallonie Bruxelles and ULiège (ARC project DREAMS G.A. 21/25-11). Z.Z. acknowledges the research program "Materials for the Quantum Age" (QuMat) for financial support. This program (Registration No. 024.005.006) is part of the Gravitation program financed by the Dutch Ministry of Education, Culture and Science (OCW). We acknowledge PRACE computing time on MareNostrum4 at Barcelona Supercomputing Center (OptoSpin id. 2020225411).

## AUTHOR DECLARATIONS

### Conflict of Interest

The authors have no conflicts to disclose.

### Author Contributions

K.-J.T. conceived the idea and concept of this work, and coordinated and supervised it; J.D.M. designed and built the spatiotemporal microscope, with input from K.-J.T., A.B. and S.V.; S.V. and J.D.M. performed the measurements, with input from A.B. and P.W., supervised by K.-J.T. and N.F.v.H.; S.V. performed the simulations and data analysis with input from A.B., J.D.M. and K.-J.T.; S.V. and D.S.R. prepared the samples; R.F. performed the *ab initio* simulations, with input from M.V., P.O. and Z.Z.; S.V., J.D.M. and K.-J.T. wrote the manuscript, with input from all authors.

**Sebin Varghese:** Data curation (lead); Formal analysis (lead); Investigation (lead); Methodology (equal); Software (lead); Validation (equal); Visualization (equal); Writing – original draft (equal); Writing – review & editing (equal). **Jake Dudley Mehew:** Investigation (equal); Methodology (equal); Supervision (supporting); Visualization (supporting); Writing – original draft (supporting); Writing – review & editing (supporting). **Alexander Block:** Investigation (equal); Methodology (equal); Software (equal); Writing – review & editing (supporting). **David Saleta Reig:** Investigation (supporting); Methodology (supporting); Resources (supporting); Writing – review & editing (supporting). **Paweł Woźniak:** Investigation (supporting); Methodology (supporting); Writing – review & editing (supporting). **Roberta Farris:** Investigation (supporting); Software (equal); Validation (supporting); Writing – review & editing (supporting). **Zeila Zanolli:** Validation (supporting); Writing – review & editing (supporting). **Pablo Ordejón:** Supervision (supporting); Writing – review & editing (supporting). **Mathieu J. Verstraete:** Supervision (supporting); Writing – review & editing (supporting). **Niek F. van Hulst:** Funding acquisition (supporting); Supervision (supporting); Writing – review & editing (supporting). **Klaas-Jan Tielrooij:** Conceptualization (lead); Funding acquisition

(lead); Investigation (lead); Methodology (lead); Project administration (lead); Supervision (lead); Writing – original draft (lead); Writing – review & editing (lead).

## DATA AVAILABILITY

The data that support the findings of this study are available within the article and its [supplementary material](#). Additional data related to this paper are available from the corresponding author upon reasonable request.

## REFERENCES

- 1 B. A. Ruzicka, L. K. Werake, H. Samassekou, and H. Zhao, "Ambipolar diffusion of photoexcited carriers in bulk GaAs," *Appl. Phys. Lett.* **97**, 262119 (2010).
- 2 M. M. Gabriel, J. R. Kirschbrown, J. D. Christesen, C. W. Pinion, D. F. Zigler, E. M. Grumstrup, B. P. Mehl, E. E. M. Cating, J. F. Cahoon, and J. M. Papanikolas, "Direct imaging of free carrier and trap carrier motion in silicon nanowires by spatially-separated femtosecond pump-probe microscopy," *Nano Lett.* **13**, 1336–1340 (2013).
- 3 N. Kumar, Q. Cui, F. Ceballos, D. He, Y. Wang, and H. Zhao, "Exciton diffusion in monolayer and bulk MoSe<sub>2</sub>," *Nanoscale* **6**, 4915–4919 (2014).
- 4 Y. Wan, Z. Guo, T. Zhu, S. Yan, J. Johnson, and L. Huang, "Cooperative singlet and triplet exciton transport in tetracene crystals visualized by ultrafast microscopy," *Nat. Chem.* **7**, 785–792 (2015).
- 5 A. Block, M. Liebel, R. Yu, M. Spector, Y. Sivan, F. J. García de Abajo, and N. F. van Hulst, "Tracking ultrafast hot-electron diffusion in space and time by ultrafast thermomodulation microscopy," *Sci. Adv.* **5**, eaav8965 (2019).
- 6 J. Sung, C. Schnedermann, L. Ni, A. Sadhanala, R. Y. S. Chen, C. Cho, L. Priest, J. M. Lim, H.-K. Kim, B. Monserrat *et al.*, "Long-range ballistic propagation of carriers in methylammonium lead iodide perovskite thin films," *Nat. Phys.* **16**, 171–176 (2020).
- 7 M. Seitz, A. J. Magdaleno, N. Alcázar-Cano, M. Meléndez, T. J. Lubbers, S. W. Walraven, S. Pakdel, E. Prada, R. Delgado-Buscalioni, and F. Prins, "Exciton diffusion in two-dimensional metal-halide perovskites," *Nat. Commun.* **11**, 2035 (2020).
- 8 A. Block, A. Principi, N. C. H. Hesp, A. W. Cummings, M. Liebel, K. Watanabe, T. Taniguchi, S. Roche, F. H. L. Koppens, N. F. van Hulst, and K.-J. Tielrooij, "Observation of giant and tunable thermal diffusivity of a Dirac fluid at room temperature," *Nat. Nanotechnol.* **16**, 1195–1200 (2021).
- 9 C. Kittel, *Introduction to Solid State Physics* (Wiley, 2004).
- 10 X. C. Tong, *Advanced Materials for Thermal Management of Electronic Packaging* (Springer Science & Business Media, 2011), Vol. 30.
- 11 H. R. Shanks, P. D. Maycock, P. H. Sidles, and G. C. Danielson, "Thermal conductivity of silicon from 300 to 1400 K," *Phys. Rev.* **130**, 1743 (1963).
- 12 H. R. Gutiérrez, N. Perea-López, A. L. Elías, A. Berkdemir, B. Wang, R. Lv, F. López-Urías, V. H. Crespi, H. Terrones, and M. Terrones, "Extraordinary room-temperature photoluminescence in triangular WS<sub>2</sub> monolayers," *Nano Lett.* **13**, 3447–3454 (2013).
- 13 G. P. Neupane, M. D. Tran, S. J. Yun, H. Kim, C. Seo, J. Lee, G. H. Han, A. K. Sood, and J. Kim, "Simple chemical treatment to n-dope transition-metal dichalcogenides and enhance the optical and electrical characteristics," *ACS Appl. Mater. Interfaces* **9**, 11950–11958 (2017).
- 14 V. Babacic, D. Saleta Reig, S. Varghese, T. Vasileiadis, E. Coy, K. J. Tielrooij, and B. Graczykowski, "Thickness-dependent elastic softening of few-layer free-standing MoSe<sub>2</sub>," *Adv. Mater.* **33**, 2008614 (2021).
- 15 P. Jiang, X. Qian, X. Gu, and R. Yang, "Probing anisotropic thermal conductivity of transition metal dichalcogenides MX<sub>2</sub> (M = Mo, W and X = S, Se) using time-domain thermoreflectance," *Adv. Mater.* **29**, 1701068 (2017).
- 16 S. Varghese, D. Saleta Reig, J. Dudley Mehew, A. Block, A. El Sachat, E. Chávez-Ángel, M. Sledzinska, B. Ballesteros, C. M. Sotomayor Torres, and K.-J. Tielrooij, "Fabrication and characterization of large-area suspended MoSe<sub>2</sub> crystals down to the monolayer," *J. Phys.: Mater.* **4**, 046001 (2021).

- <sup>17</sup>Q. Cui, F. Ceballos, N. Kumar, and H. Zhao, "Transient absorption microscopy of monolayer and bulk WSe<sub>2</sub>," *ACS Nano* **8**, 2970–2976 (2014).
- <sup>18</sup>N. Dong, Y. Li, Y. Feng, S. Zhang, X. Zhang, C. Chang, J. Fan, L. Zhang, and J. Wang, "Optical limiting and theoretical modelling of layered transition metal dichalcogenide nanosheets," *Sci. Rep.* **5**, 14646 (2015).
- <sup>19</sup>Y. Niu, S. Gonzalez-Abad, R. Frisenda, P. Marauhn, M. Drüppel, P. Gant, R. Schmidt, N. Taghavi, D. Barcons, A. Molina-Mendoza *et al.*, "Thickness-dependent differential reflectance spectra of monolayer and few-layer MoS<sub>2</sub>, MoSe<sub>2</sub>, WS<sub>2</sub> and WSe<sub>2</sub>," *Nanomaterials* **8**, 725 (2018).
- <sup>20</sup>W. Zhao, Z. Ghorannevis, L. Chu, M. Toh, C. Kloc, P.-H. Tan, and G. Eda, "Evolution of electronic structure in atomically thin sheets of WS<sub>2</sub> and WSe<sub>2</sub>," *ACS Nano* **7**, 791–797 (2013).
- <sup>21</sup>N. B. Mohamed, H. E. Lim, F. Wang, S. Koirala, S. Mouri, K. Shinokita, Y. Miyauchi, and K. Matsuda, "Long radiative lifetimes of excitons in monolayer transition-metal dichalcogenides MX<sub>2</sub> (M = Mo, W; X = S, Se)," *Appl. Phys. Express* **11**, 015201 (2017).
- <sup>22</sup>M. Selig, G. Berghäuser, A. Raja, P. Nagler, C. Schüller, T. F. Heinz, T. Korn, A. Chernikov, E. Malic, and A. Knorr, "Excitonic linewidth and coherence lifetime in monolayer transition metal dichalcogenides," *Nat. Commun.* **7**, 13279 (2016).
- <sup>23</sup>P. A. G. O'hare, W. N. Hubbard, G. K. Johnson, and H. E. Flotow, "Calorimetric measurements of the low-temperature heat capacity, standard molar enthalpy of formation at 298.15 K, and high-temperature molar enthalpy increments relative to 298.15 K of tungsten disulfide (WS<sub>2</sub>), and the thermodynamic properties to 1500 K," *J. Chem. Thermodyn.* **16**, 45–59 (1984).
- <sup>24</sup>A. V. Blinder, A. S. Bolgar, and Z. A. Trofimova, "Thermodynamic properties of selenides of transition metals," *Powder Metall. Met. Ceram.* **32**, 234–239 (1993).
- <sup>25</sup>D. Saleta Reig, S. Varghese, R. Farris, A. Block, J. D. Mehew, O. Hellman, P. Woźniak, M. Sledzinska, A. El Sachat, E. Chávez-Ángel *et al.*, "Unraveling heat transport and dissipation in suspended MoSe<sub>2</sub> from bulk to monolayer," *Adv. Mater.* **34**, 2108352 (2022).
- <sup>26</sup>H. Zobeiri, R. Wang, T. Wang, H. Lin, C. Deng, and X. Wang, "Frequency-domain energy transport state-resolved Raman for measuring the thermal conductivity of suspended nm-thick MoSe<sub>2</sub>," *Int. J. Heat Mass Transfer* **133**, 1074–1085 (2019).
- <sup>27</sup>J. Liu, G.-M. Choi, and D. G. Cahill, "Measurement of the anisotropic thermal conductivity of molybdenum disulfide by the time-resolved magneto-optic Kerr effect," *J. Appl. Phys.* **116**, 233107 (2014).
- <sup>28</sup>P. Yuan, R. Wang, T. Wang, X. Wang, and Y. Xie, "Nonmonotonic thickness-dependence of in-plane thermal conductivity of few-layered MoS<sub>2</sub>: 2.4 to 37.8 nm," *Phys. Chem. Chem. Phys.* **20**, 25752–25761 (2018).
- <sup>29</sup>R. Wang, T. Wang, H. Zobeiri, P. Yuan, C. Deng, Y. Yue, S. Xu, and X. Wang, "Measurement of the thermal conductivities of suspended MoS<sub>2</sub> and MoSe<sub>2</sub> by nanosecond ET-Raman without temperature calibration and laser absorption evaluation," *Nanoscale* **10**, 23087–23102 (2018).
- <sup>30</sup>A. Pisoni, J. Jacimovic, R. Gaál, B. Náfrádi, H. Berger, Z. Révay, and L. Forró, "Anisotropic transport properties of tungsten disulfide," *Scr. Mater.* **114**, 48–50 (2016).
- <sup>31</sup>A. S. Bolgar, Z. A. Trofimova, and A. A. Yanaki, "Thermodynamic properties of tungsten diselenide in a broad temperature range," *Sov. Powder Metall. Met. Ceram.* **29**, 382–385 (1990).
- <sup>32</sup>L. S. Volovik, V. V. Fesenko, A. S. Bolgar, S. V. Drozdova, L. A. Klochkov, and V. F. Primachenko, "Enthalpy and heat capacity of molybdenum disulfide," *Sov. Powder Metall. Met. Ceram.* **17**, 697–702 (1978).
- <sup>33</sup>D. O. Lindroth and P. Erhart, "Thermal transport in van der Waals solids from first-principles calculations," *Phys. Rev. B* **94**, 115205 (2016).
- <sup>34</sup>A. Cepellotti, G. Fugallo, L. Paulatto, M. Lazzeri, F. Mauri, and N. Marzari, "Phonon hydrodynamics in two-dimensional materials," *Nat. Commun.* **6**, 6400 (2015).
- <sup>35</sup>S. Lee, D. Broido, K. Esfarjani, and G. Chen, "Hydrodynamic phonon transport in suspended graphene," *Nat. Commun.* **6**, 6290 (2015).
- <sup>36</sup>X. Xu, L. F. C. Pereira, Y. Wang, J. Wu, K. Zhang, X. Zhao, S. Bae, C. Tinh Bui, R. Xie, J. T. L. Thong *et al.*, "Length-dependent thermal conductivity in suspended single-layer graphene," *Nat. Commun.* **5**, 3689 (2014).